

Nanoscale

Accepted Manuscript

This article can be cited before page numbers have been issued, to do this please use: B. Freis, C. Kiefer, M. D. L. A. Ramirez, S. Harlepp, D. Mertz, B. Pichon, C. Iacovita, S. Laurent and S. Begin-Colin, *Nanoscale*, 2024, DOI: 10.1039/D4NR01397B.



This is an Accepted Manuscript, which has been through the Royal Society of Chemistry peer review process and has been accepted for publication.

Accepted Manuscripts are published online shortly after acceptance, before technical editing, formatting and proof reading. Using this free service, authors can make their results available to the community, in citable form, before we publish the edited article. We will replace this Accepted Manuscript with the edited and formatted Advance Article as soon as it is available.

You can find more information about Accepted Manuscripts in the [Information for Authors](#).

Please note that technical editing may introduce minor changes to the text and/or graphics, which may alter content. The journal's standard [Terms & Conditions](#) and the [Ethical guidelines](#) still apply. In no event shall the Royal Society of Chemistry be held responsible for any errors or omissions in this Accepted Manuscript or any consequences arising from the use of any information it contains.

Defects or not defects? Or how to design 20 - 25 nm spherical iron oxide nanoparticles to harness both magnetic hyperthermia and photothermia

View Article Online
DOI: 10.1039/D4NR01397B

Barbara Freis^{1,2}, Céline Kiefer¹, Maria de los Angeles Ramirez¹, Sébastien Harlepp^{3,4,5}, Damien Mertz¹, Benoit Pichon¹, Cristian Iacovita^{6,*}, Sophie Laurent², Sylvie Bégin^{1,*}

1 - Université de Strasbourg, CNRS, Institut de Physique et Chimie des Matériaux, UMR CNRS-UdS 7504, 23 Rue du Loess, BP 43, 67034 Strasbourg, France

2 - Laboratoire de NMR et d'imagerie moléculaire, Université de Mons, Avenue Maistriau 19, 7000 Mons, Belgium

3- Institut de Cancérologie Strasbourg Europe, 67000 Strasbourg, France

4 - Equipe Labellisée Ligue Contre le Cancer

5 - Strasbourg Drug Discovery and Development Institute (IMS), 67000 Strasbourg, France

6 - Department of Pharmaceutical Physics-Biophysics, Faculty of Pharmacy, Iuliu Hatieganu University of Medicine and Pharmacy, 6 Pasteur St., 400349 Cluj-Napoca, Romania

Corresponding authors: sylvie.begin@unistra.fr; cristian.iacovita@umfcluj.ro

Abstract:

Designing iron oxide nanoparticles (IONPs) to effectively combine magnetic hyperthermia (MH) and photothermia (PTT) in one IONPs formulation presents a significant challenge to ensure a multimodal therapy allowing to adapt the treatment to each patient. Recent research has highlighted the influence of factors such as size, shape, and the amount of defects on both therapeutic approaches. In this study, 20-25 nm spherical IONPs with a spinel composition were synthesized by adapting the protocol of the thermal decomposition method to control the amount of defects. By tuning different synthesis parameters such as the precursor nature, the introduction of a well-known oxidizing agent, dibenzylether (DBE), in the reaction medium, the heating rate and duration and the introduction of a nucleation step, we established thus two different synthesis protocols, one involving the use of a small amount of DBE leading to IONPs with only few defects and another that took an optimized route to oxidize the wüstite nuclei during the IONPs growth and led to IONPs displaying more structural and oxygen defects.

IONPs exhibiting fewer defects displayed enhanced MH and PTT heating values and even when immobilized in a matrix, despite a decrease in MH heating values showing that they release mainly heat through the Brownian mechanism. These MH measurements have also confirmed that defects play a key role to enhance Néel relaxation. PTT measurements demonstrated higher heating values with IONPs with fewer defects and a correlation between Urbach energy and SAR values suggesting an impact of vacancies defects on PTT performances. Therefore, IONPs displaying fewer defects in our synthesis conditions appear as suitable IONPs to combine both MH and PTT treatments with high performances. These findings pave the way for promising applications in combined therapies for cancer treatment.



I. Introduction

View Article Online
DOI: 10.1039/D4NR01397B

Spherical spinel iron oxide nanoparticles (IONPs) with sizes in the range 20-25 nm are promising for magnetic hyperthermia (MH) when the size of IONPs has less impact for photothermia (PTT) performance¹⁻⁶. In MH, IONPs, upon exposure to an alternating magnetic field (AMF), generate localized heat effective against cancer cells, which are more sensitive to temperature increases than healthy cells⁷⁻¹⁰. However, MH's efficacy is hindered by limited heating power, often requiring high local doses of IONPs^{2,7,11-13}. Enhancing IONPs performance is crucial and is generally achieved through increasing saturation magnetization (M_s) and effective anisotropy^{2,8,14-16}. Larger-sized IONPs exhibit higher M_s improving MH efficiency^{2,11,16,17}. Despite their promise, IONPs of 20-25 nm were shown to primarily release heat through Brownian relaxation rather than Neel relaxation, which diminishes their efficacy when located within cells or tissues^{9,18-22}. Factors such as NP aggregation and immobilization upon interaction with cells contribute to this decrease, affecting their MH efficiency^{8,17-2}. Additionally, defects within IONPs have been reported to improve MH performance by favoring Neel relaxation in cellular environments²³⁻²⁵.

Recent studies have shown that IONPs are also effective for photothermal therapy (PTT) by converting absorbed light into localized heating when exposed to near-infrared laser irradiation. This process would be facilitated by d-d electron transitions, moving electrons from conduction to valence bands²⁶. Since Yu et al.'s initial report in 2011²⁷, IONPs have consistently proven being efficient in generating heat under laser irradiation^{4,5,26,28,29}. Factors influencing heat release remain somewhat unclear. While some studies suggest that IONP shape affects heating^{4,5}, others argue that crystallographic structure, rather than size or shape, is the primary determinant of PTT effectiveness^{6,26,29,30}. Bertuit et al.³⁰ examined iron oxide nanoflowers with varying levels of defects and found that excessive defects (oxygen vacancies) led to diminished PTT performance. They attributed this behavior to the trapping of electrons by oxygen vacancies, hindering electron transfer responsible for heat generation.

The recent use of IONPs as PTT nano-heaters offers a novel dual treatment method by combining MH and PTT. This approach benefits from a reduced IONPs dose and enhanced MH through laser irradiation. 20-25 nm iron oxide-based nanospheres hold potential for merging MRI and hyperthermia therapy, including PTT and MH. However, the presence of defects appears to have an antagonist effect on both MH and PTT. Two main type of defects have been noticed: oxygen vacancies defects as reported by Bertuit et al.³⁰ or structural defects such as dislocation and/or antiphase boundaries. The presence of a wüstite core is often observed using the thermal decomposition method, (especially when targeting IONPs with a mean size higher than 15 nm) as the nuclei exhibit a wüstite composition^{31,32}. Structural defects have been reported to form during the oxidation of $Fe_{1-x}O$ in the magnetite phase^{7,11,33}. Indeed, our previous studies on core-shell $Fe_{1-x}O@Fe_{3-x}O_4$ nanocubes^{33,34} and the work of Wetterskog et al.³⁵ have shown that the post-oxidation of $Fe_{1-x}O$ induced the formation of lattice dislocations and/or antiphase boundaries in NPs. Dibenzyl ether has been demonstrated to be an effective oxidizing agent^{7,36,37} either used as solvent or added to the reaction medium. However, to obtain IONPs with a mean size higher than 15nm, as the core is wüstite, there is a competition between the growth and oxidation kinetics, which may be tuned by adjusting synthesis conditions³¹.



This work investigates the influence of synthesis parameters and dibenzyl-ether (DBE) quantity on the characteristics of iron oxide nanoparticles (IONPs), focusing on size, composition, and defect levels. The challenge lies in consistently producing, using the thermal decomposition method, spherical IONPs in the range 20-25 nm able to combine both MH and PTT therapies. Our aim is to adapt this synthesis method by tuning synthesis parameters to obtain IONPs with precise control over composition and defect levels. Defects, stemming from oxidation processes, including oxygen vacancies and structural irregularities, are crucial in determining the efficiency of MH and PTT combination. We analyze the impact of various parameters like precursor nature, reaction temperature, heating rate, and DBE amount on IONPs characteristics. Both homemade and commercial iron stearates, along with different DBE levels, influence the size, composition, and defects of the IONPs. Additionally, an oxidation treatment on core-shell IONPs yields promising results for magnetic and MH properties. Our goal is to design IONPs capable of effectively combining PTT and MH treatments, assessed separately through MH and PTT performance evaluations.

II Materials and methods

II.1. Materials

Iron stearate (FeSt_3) was either homemade^{12,38,39} from sodium stearate (purity 98.8%) purchased from TCI and ferric chloride (purity 99%) purchased from Sigma Aldrich, or directly purchased from TCI (purity min 60% of stearic acid, 5.8 to 7% of iron and maximum 10% of free acid). Acetone (purity 99.8%), chloroform (purity 99%), hexane (purity 99%) and THF (purity 99.5%) were purchased from Carlo Erba. Dioctyl ether (OE) (purity 99%) was purchased from Sigma-Aldrich. Oleic acid (OA) (purity 99%) was purchased from Alfa Aesar. Dibenzylether (DBE) (purity 98%) and squalane (purity 99%) were purchased from ACROS Organics. The dendron D1-2P was provided by Superbranche.

II.2. Precursor synthesis

Iron stearate (III) was synthesized by precipitating sodium stearate (NaSt) and ferric chloride (FeCl_3) salts in water¹². Sodium stearate (9.8 g, 32 mmol) was dissolved in distilled water (80 mL) in a round-bottomed flask, heated to reflux, and stirred until fully dissolved. Separately, ferric chloride (2.88 g, 10.6 mmol) was dissolved in water (40 mL) and added to the sodium stearate solution with vigorous stirring, resulting in immediate formation of a light orange precipitate. After 15 minutes of stirring at this temperature, the solution was cooled to room temperature. The precipitate was washed once by centrifugation (14,000 rpm, 10 min), then filtered with a Büchner funnel and oven-dried at 65°C for 24 hours, yielding approximately 9 g of precursor. One batch of precursor was sufficient for four 20 nm IONPs syntheses.

II.3. 20 nm spherical IONPs synthesis

For 20 nm spherical IONPs synthesis several protocols were tested and are discussed in this work. Only the two main protocols for the synthesis of reproducible 20 nm spherical NPs are described hereafter. All the syntheses were performed in air.

Protocol P20_1: 2.2 mmol of FeSt_3 (1.99 g), 4.4 mmol of OA (1.24 g) were mixed with squalane (15.8 g, 19.5 mL) and 2.6 mmol of dibenzylether (0.53 g, 0.5 mL) in a two-neck round-bottom-flask of 100 mL. The mixture was first heated to 120°C (heating device temperature: 130°C) for 60 min to dissolve the reagents in squalane. After this step, the condenser was connected to the flask and the



mixture was heated up to 330°C (heating device temperature: 360°C) with a 5°C/min ramp. The mixture was refluxed at 330°C for 120 min. The obtained black NPs suspension was cooled down to 100°C to proceed to the washing step.

Protocol P20_2: 2.0 mmol of FeSt₃ (1.85 g), 6.7 mmol of OA (1.90 g) were mixed with squalane (15.8 g, 19.5 mL) and 2.6 mmol of dibenzylether (0.53 g, 0.5 mL) in a two-neck round-bottom-flask of 100 mL. The mixture was first heated to 120°C (heating device temperature: 130°C) for 60 min to dissolve the reagents in squalane. After this step, the condenser was connected to the flask and the mixture was heated up to 330°C (heating device temperature: 360°C) with a 5°C/min ramp. The mixture was refluxed at 330°C for 60 min. The obtained black NPs suspension was cooled down to 100°C to proceed to the washing step.

Protocol P20_3_no_DBE: 2.0 mmol of FeSt₃ (1.85 g), 6.7 mmol of OA (1.90 g) were mixed with squalane (16.2 g, 20 mL) in a two-neck round-bottom-flask of 100 mL. The mixture was first heated to 120°C (heating device temperature: 130°C) for 60 min to dissolve the reagents in squalane. After this step, the condenser was connected to the flask and the mixture was heated up to 280°C (heating device temperature: 310°C) with a 5°C/min ramp. The mixture was refluxed at 280°C for 30 min. After this step, the condenser was connected to the flask and the mixture was heated up to 330°C (heating device temperature: 360°C) with a 1°C/min ramp. The mixture was refluxed at 330°C for 60 min. The obtained black NPs suspension was cooled down to 100°C to proceed to the washing step.

Washing step: The same washing step was performed on NPs synthesized from either protocol P20_DBE or P20_NO_DBE. 10 mL of chloroform were added to the IONPs suspension at a temperature around 100°C. Then, this suspension was introduced in a flask containing 400 mL of acetone. This mixture was put on a magnet to collect the IONPs and discard the supernatant. The collected IONPs were redispersed in 50 mL of chloroform. 400 mL of acetone were added again to proceed to a washing step: the mixture was heated at 60°C for 45 min under mechanical stirring. At the end, the IONPs were collected with a magnet and the supernatant was discarded. Finally, the IONPs were resuspended in 40 mL of THF for their storage or further utilization.

II.4. Oxidation process of core-shell IONPs

5 ml of a suspension of core-shell IONPs (Fe_{1-y}O@Fe_{3-x}O₄) suspended in THF were mixed with 5 mL dioctylether and 0.5 g OA in a two-neck round-bottom-flask of 100 mL. The mixture was heated to 120°C (heating device temperature: 130°C) for 30 min and the IONPs were resuspended in 10 mL of THF for their storage or further utilization.

II.5. Dendronization step

After synthesis, the IONPs are coated with OA and suspended in THF. Subsequently, a ligand exchange is performed in THF to replace the OA with dendron molecules. The dendron is composed of a bi-phosphonate anchoring group to ensure a robust link to the NPs surface, three PEG chains for biocompatibility and stability in water (Figure S1). The central PEG chain is longer and terminated with a carboxylate function, enabling the attachment of additional molecules such as dyes or targeting ligands [44]. The ligand exchange between OA and the dendron (D1-2P) (Figure S1) was performed in THF. Briefly, 5 mL of IONPs@OA at 1 mg Fe/mL were stirred for 48 hours with 10 mg of dendron. To maximize the ligand exchange and remove most of oleic acid molecules, the suspension is then purified by ultrafiltration. After that, 5 mg of dendron are added to the mixture for another 48 hours of stirring. The suspension was mixed with hexane (volume ratio 1/3:2/3) to precipitate the



DNPs. The suspension was centrifuged at 8000 rpm for 5 min and the supernatant was discarded. Finally, the DNPs are collected and dispersed in deionized water. The water suspension is purified by ultrafiltration 3 times.

View Article Online
DOI: 10.1039/D4NR01397B

II.6. Characterization techniques

Fourier-Transform Infrared Spectroscopy (FTIR): standard infrared spectra were recorded between 4000 cm^{-1} and 400 cm^{-1} with FTIR spectrometer, Spectrum 100 from Perkin Elmer on both iron precursors and IONPs samples. The samples were ground and diluted in a non-absorbent KBr matrix before their analysis. The iron precursor powders were characterized by attenuated total reflectance (ATR) FTIR spectroscopy to examine their main bands corresponding to alkyl chains (peaks between 2800 cm^{-1} and 3000 cm^{-1} , "iron" in iron stearate (a band at 720 cm^{-1}) and carboxylate-based groups (between 1700 cm^{-1} and 1300 cm^{-1}). The FTIR spectra of IONPs samples allowed to assess the presence of the characteristic band corresponding to the spinel structure between 800 cm^{-1} and 400 cm^{-1} , the presence of the characteristic bands of oleic acid (alkyl bands between 3000 cm^{-1} and 2800 cm^{-1}) and more importantly, the disappearance of the characteristic band of the iron precursor at 720 cm^{-1} .

Thermogravimetric analysis (TGA): to investigate the thermal decomposition of the different batches of FeSt_3 , TGA coupled with differential thermal analysis (DTA) is performed on dried powder samples from 20 to 600 $^{\circ}\text{C}$ at 5 $^{\circ}\text{C}/\text{min}$ under air by using an SDJ Q600 apparatus. Differential thermogravimetric measurements were obtained after a first-order differentiation calculation using an OriginLab Software.

Transmission electron microscopy (TEM): to have access to their size and morphology, the IONPs were characterized by TEM with a JEOL 2013 microscope operating at 200 kV (point resolution 0.18 nm). The size distribution of NPs was estimated from the size measurements of more than 300 nanoparticles using ImageJ software. High-resolution (HR-TEM) images were also recorded to analyze crystallographic plans and to check the amount of structural defects.

X-ray diffraction (XRD): the XRD patterns allow identifying the crystalline phases of as synthesized IONPs. It is a quick way to identify core-shell nanoparticles with the characteristic peaks of the wüstite phase. However, it is more complicated to differentiate maghemite from magnetite as they display similar XRD patterns. Refinement of the XRD patterns is thus necessary to compare the lattice parameter of the IONPs to those of magnetite and maghemite phases and to check if the composition is closer to that of maghemite or magnetite. Briefly, IONPs suspended in organic solvent (chloroform or THF) were dried on XRD silicon sample holders. The XRD patterns were collected at room temperature with a Bruker D8 Discover diffractometer in Bragg Brentano geometry equipped with a monochromatic copper radiation source ($K\alpha_1 = 0.154056 \text{ nm}$) and an energy-resolved Lynx-Eye XE-T detector in the 25–65 $^{\circ}$ (2θ) range with a scan step of 0.03 $^{\circ}$. High-purity silicon powder ($a = 0.543082 \text{ nm}$) was used as an internal standard. The diffraction patterns were refined by LeBail's method using the Fullprof software. The background, modeled as a linear function based on 20 experimental points, was refined, as well as the zero shift. The peaks were modeled with the modified Thompson-Cox-Hasting (TCH) pseudo-Voigt profile function.

X-ray photoelectron spectroscopy (XPS): to assess the chemical bonds, present on the IONPs surface, XPS was performed on various suspensions. The X-ray photoelectron spectroscopy (XPS) measurements were performed on a Thermo VG spectrometer, using Al $K\alpha$ radiation ($h\nu = 1486.6$



eV). Survey and high-resolution spectra were recorded in constant pass energy mode (100 and 20 eV respectively). The binding energy scale was corrected for electrostatic charging using the C 1s peak of adventitious carbon at 284.6 eV as an internal reference.

Ultraviolet-visible-near-infrared spectroscopy (UV-vis): to determine defects levels in various IONPs batches, ultraviolet-visible-near-infrared (UV-vis-NIR) spectroscopy was performed to determine the band gap energy E_g of the samples and their Urbach energy E_u (see SI part). UV-vis-NIR spectra of IONPs suspension at a concentration of 0.05 mg Fe/mL in chloroform, were recorded between 1100 nm and 250 nm at room temperature in a 1 cm³ quartz cuvette using a Lambda 950 UV-vis Spectrometer by Perkin Elmer.

Dynamic Light Scattering (DLS) and Zeta Potential: DLS measurements were performed on a MALVERN (nano ZetaSizer) equipment to assess the colloidal stability of the IONPs suspension in organic solvent or of DNPs in water and to determine their mean hydrodynamic diameter (D_h). The zeta potential was recorded using the same equipment. The coupling of the TL was confirmed by an increase of D_h and a change in zeta potential values.

Magnetic measurements: magnetic measurements were conducted using a superconducting Quantum Interference Device (SQUID) magnetometer (MPMS SQUID VSM). To prepare the samples, 50 μ L of a known concentration suspension of IONPs in chloroform or THF were introduced in a special capsule, which served as the sample holder for the SQUID apparatus. The solvent was let to evaporate. This process was repeated until we achieved a uniform layer of dried IONPs covering the bottom of the capsule. We then proceeded to record zero-field-cooled (ZFC) and field-cooled (FC) curves as follows: the sample within the SQUID apparatus was initially cooled to 5 K with no applied magnetic field following a degaussing procedure. Subsequently, we applied a magnetic field of 7.5 mT and recorded the magnetization as the sample was heated from 5 K to 300 K (ZFC). Afterward, we cooled the sample down to 5 K while maintaining the same applied magnetic field, and we recorded the magnetization as the sample was heated from 5 K to 300 K (FC). In addition to this, we also recorded hysteresis loops at 300 K, and these were plotted as a function of the weight of iron oxide present in the capsule.

Magnetic Hyperthermia and specific absorption rate (SAR) evaluation: SAR of each type of IONPs suspended in water or solid matrix (polyethylene glycol 8000 – PEG 8K) were measured by the calorimetry method. This method involves recording the temperature of the sample during 10 minutes when subjected to alternating magnetic field (AFM). The device used is a EasyHeat 1.2 kW Induction Heating System from Ambrell. With this system the amplitude of AFM can be varied from 0 to 65 kA.m⁻¹ while the AFM frequency was set to 355 kHz. Vials adapted for MH measurements are filled with 0.5 mL of colloidal suspension at an iron concentration of 1 mg/mL. The heating curves were fitted with the Box-Lucas equation:

$$\Delta T = (S_m/k)(1 - \exp(-k(t-t_0)))$$

where the fitting parameters S_m and k are the initial slope of the heating curve and the constant describing the cooling rate, respectively. The SAR can be calculated as:

$$SAR = (c m S_m) / m_{Fe}$$

where c is the specific heat of colloid (water is 4186.8 J.kg⁻¹.K⁻¹ and PEG 8k is 2135.27 J.kg⁻¹.K⁻¹), m = ρV is the mass of colloid, taken as the product between the density (water is 0.997 g.cm⁻³ and PEG8k is 1.0832 g.cm⁻³) and the volume and m_{Fe} is the mass of iron in the sample. IONPs, dispersed in water at the desired concentrations, were collected at the bottom of the vial by a magnet, the water was



removed and hot liquid PEG 8 k (80°C) was introduced. The dispersion of IONPs on the entire volume of the sample was ensured by immediate sonication with a probe sonicator, following by sodification without/with the application of static magnetic field of 65 kA.m⁻¹ generated by two cubic neodymium magnets with a 3 cm side length.

Photothermia and SAR evaluation: 2 mL of a known concentration of IONPs suspension was placed in a 1 cm³ quartz cuvette (if IONPs suspended in organic solvent) or plastic cuvette (if IONPs suspended in aqueous medium) and irradiated for 5 min thanks to a near-infrared laser at 1064 nm and a power of 1W.cm⁻². A thermal probe was put inside the cuvette to record the temperature during irradiation. After irradiation, the temperature increase as a function of time was plotted and the associated specific absorption rate (SAR) in W.g⁻¹ was calculated from the experimental curve as described below. As an analogy to the magnetothermal transfer, the photothermal transfer can be calculated as the specific absorption rate (SAR) in watts per gram of iron oxide absorbing NIR light. This value was calculated by a calorimetric method. By plotting the temperature profiles of the NPs' suspensions subjected to NIR light and then adjusting the experimental curve with a polynomial function, the $[\frac{dT}{dt}]_{t=0, \text{solvent}}$ can be determined. In order to perform precise calculations, the contribution of the solvent in the temperature elevation has to be removed. The calculation of the SAR is thus summed up as:

$$SAR = m_s \frac{C_s}{m_{Fe_3O_4}} \times \left(\left[\frac{dT}{dt} \right]_{t=0} - \left[\frac{dT}{dt} \right]_{t=0, \text{solvent}} \right)$$

where m_s and C_s are respectively the mass (in g) and the heat capacity (in J.g⁻¹.K⁻¹) of the sample, $m_{Fe_3O_4}$ (in g) is the mass of iron oxide present in the sample, $[\frac{dT}{dt}]_{t=0, \text{solvent}}$ the derivative function of the solvent. Both of these derivatives are determined the same way as for MH (*i.e.*, a second order polynomial fit of the temperature curve).

III. Results

III.1 Effect of the FeSt₃ precursor and of the reaction temperature range on IONPs synthesis

Various synthesis parameters such as the type of precursor, solvent, and ratio were investigated to establish an optimal synthesis protocol for producing 20 nm spherical IONPs^{31,38,39}. However, there is still a need to understand how to achieve greater reproducibility in size, composition and defects across multiple synthesis attempts. Two iron stearate precursors, namely FeSt₂ and FeSt₃, with molar ratio of Fe:St at 1:2 and 1:3, respectively, were previously examined. It was demonstrated that only FeSt₃ allowed obtaining spherical IONPs with a mean size exceeding 15 nm^{31,38}. Indeed, FeSt₂ is primarily composed of [Fe₃-(μ₃-O)St₆.xH₂O]Cl, whereas FeSt₃ is a mixture composed mainly of [Fe₇(μ₃-O(H))₆(μ₂-OH)_xSt_{12-2x}]St, [Fe₃(μ₃-O)St₆.xH₂O]St and free stearic acid. FeSt₃ displays a broaden distribution of complexes, with larger Fe complexes exhibiting greater thermal stability, which contribute to the growth step of nuclei³⁸. Consequently, the study dedicated to the synthesis of 20 nm spherical IONPs was carried out using homemade FeSt₃, synthesized through the coprecipitation of sodium stearate and ferric chloride salts in an aqueous solution, as described in^{12,38,39} and material and method section. Initially, a previously validated protocol for the synthesis of 20 nm sized IONPs with a spinel composition was replicated^{7,31}. This protocol (P20_1) involved the use of squalane - which has a boiling point (T_B = 470 °C) higher than the targeted temperature [36] - and the addition of a small amount of DBE, aiming to slightly lower the reaction temperature and to provide oxidant



species to the reaction media^{7,36,37}. Given that only a limited number of IONPs synthesis can be performed with one batch of homemade FeSt₃, such study led us to investigate the reproducibility of home-made FeSt₃ synthesis in relation to the obtained IONPs. These syntheses were thus conducted with various batches of homemade FeSt₃ (denoted as FeSt₃-1, FeSt₃-2, FeSt₃-3, FeSt₃-4) as well as with a commercial FeSt₃ (denoted as FeSt₃-TCI).

Multiple batches of synthesized IONPs underwent characterization via transmission electron microscopy (TEM) and X-ray diffraction (XRD), with results presented in Table S1. Despite attempts to maintain a setpoint temperature of 360°C for reaching a reaction temperature of 330°C, different reaction temperatures were observed, likely due to the solvent mixture's boiling point³¹. Nevertheless, the TEM mean size of IONPs remained consistent across different temperatures, ranging from 16 to 27 nm, with no correlation between size and temperature. Despite employing the same protocol, variations in mean sizes were evident among batches showing that they were in fact due to variations between home-made FeSt₃ batches.

Concerning the IONPs composition, the analysis of XRD patterns allows checking the presence of the wüstite phase and consequently of a Fe_{1-x}O@Fe_{3-x}O₄ core-shell structure. The wüstite phase displays distinct diffraction peaks at varying Bragg's positions compared to the spinel iron oxide phases, with a different lattice parameter of 4.326 Å (powder diffraction PDF file: 01-089-2468). Thus, this wüstite phase can be identified by XRD. Figure S2 illustrates a representative XRD pattern of synthesized IONPs using the P20_1 protocol and all diffraction peaks correspond only to the spinel iron oxide phase. Comparison of lattice parameters with bulk magnetite (8.396 Å, PDF file: 00-019-0629) and maghemite (8.351 Å, PDF file: 00-039-1346) indicates the composition of the NPs is closer to magnetite, as expected for NPs with such high mean sizes (Table 1)^{11,31,40}. The average crystallite sizes deduced from XRD patterns are lower than the TEM sizes which suggests strongly the presence of defects within the IONPs synthesized with the P20_1 protocol^{7,31}. Indeed, nuclei in the thermal decomposition process display often a wüstite composition which oxidation during the growth step leads to defects^{31,32,38}. In addition, at the nanoscale, Fe²⁺ at the surface of magnetite are easily oxidized leading to a core-shell structure, typical for IONPs with a mean size higher than 12 nm, consisting of a Fe_{3-x}O₄ core surrounded by an oxidized shell^{11,13}.

Significant variations in size were observed among different batches of IONPs. A detailed analysis of homemade precursor structures (detailed in SI) aimed to understand these differences. Characterizations of homemade and commercial batches (FeSt₃-TCI) revealed disparities in carboxylate coordination, polycation type, and thermal stability (Figure S3). FeSt₃ synthesis is particularly delicate due to the presence of larger iron polycations (MADI-TOFF analysis in Table S1), making consistent polycations composition control challenging. Consequently, the commercial batch was chosen for further experiments. The thermal decomposition synthesis with this commercial FeSt₃ and the P20_1 protocol at 326°C led to IONPs with a similar spinel composition, a TEM size of 23.0 ± 2.4 nm and a crystallite size of 18.3 nm. Such a discrepancy between the mean TEM and crystallite sizes was already observed in earlier studies in NPs with similar sizes^{7,31} or in nanocubes^{33,34} and that was shown to be due to the presence of structural defects by HRTEM. Such HRTEM characterization will be performed below on the most suitable NPs.

With the objective to transfer these IONPs in water and to test them for hyperthermia, attempts were made to coat them with the dendron molecule (Figure S1). We observed thus that the reaction



temperature required for synthesizing larger IONPs can impact the dendronization step. A ligand exchange was performed in THF to replace OA with dendron molecules. However, applying dendronization to 20 nm IONPs synthesized using a specific protocol resulted in large aggregates in water, indicating unsuccessful dendronization. To understand this, we compared batches from this protocol with those from a standard synthesis method for 10 nm IONPs¹¹. The main difference was the reaction temperature: the standard method heated the mixture to the boiling point of octyl ether (290°C) for two hours, while the P20_1 protocol heated the reaction mixture to 330°C for larger IONPs. We hypothesized that prolonged heating at this high temperature may degrade the Fe-OH bonds on the IONPs' surface (left part of Figure 1), leading to a phenomenon comparable to passivation and resulting in the conversion of Fe-OH bonds to bridging Fe-O-Fe, ultimately affecting the ligand exchange process.

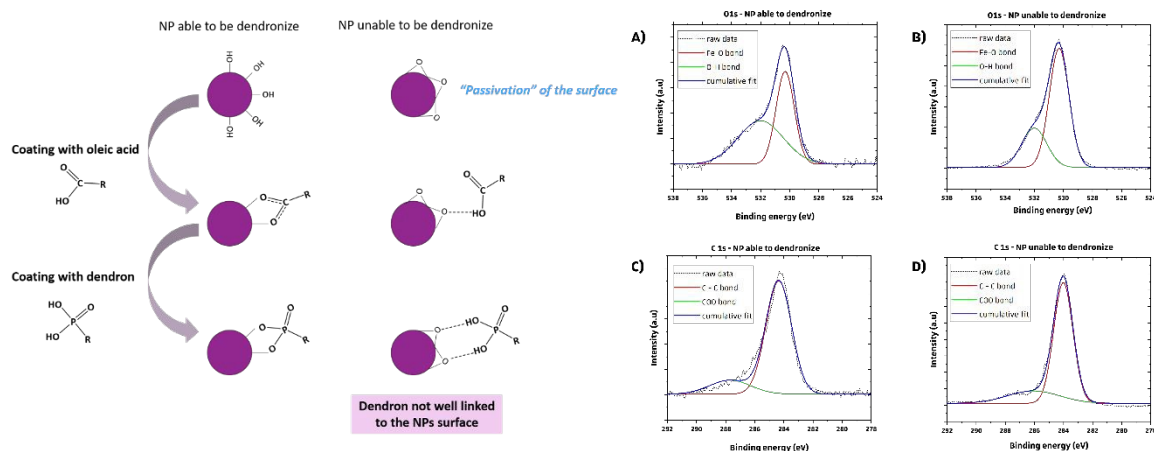


Figure 1. Left: theoretical scheme depicting the comparison of the dendronization process between two types of NPs: one with Fe-OH surface group and another NP that was synthesized at an excessively high temperature, resulting in the formation of a Fe-O-Fe bridging bond on its surface. Right: deconvoluted O1s (A and B) and C1s (C and D) spectra of two sets of NPs: capable of undergoing successful dendronization (A and C) and unable to do so (B and D).

XPS analyses were conducted to verify our hypothesis regarding the surface chemical bonds of two types of IONPs: those produced using the P20-1 protocol (at $\approx 330^\circ\text{C}$) and those synthesized via the 10 nm protocol (at 290°C). Results indicate a higher intensity of Fe-OH XPS band (peak at 532 eV) on NPs suitable for dendronization compared to those synthesized at 360°C for 2 hours (Figure 1B-D), suggesting a reduced presence of oleic acid molecules and supporting the hypothesis of a bridging Fe-O-Fe bond on their surface. Modifications to the synthesis protocol were necessary to address this dendronization challenge, involving adjustments to heating rate, reaction duration, and temperature. Further studies are needed to optimize the synthesis of 20 nm spherical IONPs for dendronization, including evaluating the role of DBE in the synthesis process.

III.2 Effect of the heating rate and reaction temperature and duration on IONPs size and composition

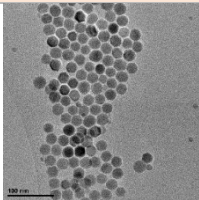
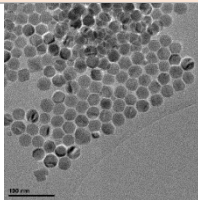
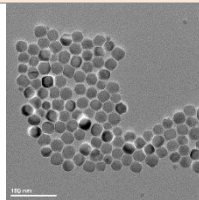
A 2-hour reaction at 330°C was shown to affect the dendronization step. To address this, two options are proposed: lowering the synthesis temperature to around 310°C or reducing the reaction



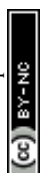
time at 330°C. Lowering the temperature significantly deviates from squalane's boiling point, complicating temperature control and compromising repeatability. It also risks preserving the wüstite core, requiring high temperatures for oxidation and nanoparticle growth. Alternatively, reducing reaction time, though intensifying competition between oxidation and growth kinetics, is more suitable. A new protocol (P20_2) decreases reaction time to one hour and adjusts the FeSt₃:OA ratio from 1:2 to 1:3. OA is recognized for its ability to stabilize the iron precursor, leading to a low yield in nuclei and thus resulting in a high concentration of monomers/precursors available for the growth step [10,39] but also it was expected to allow a better control of the reaction temperature. In addition, these specific reactant ratios and amounts have proven successful in previous studies [1,2,6].

Different batches of monodisperse spherical IONPs, named NP_P20_2_DBE_A, NP_P20_2_DBE_B and NP_P20_2_DBE_C in Table 1, were thus synthesized. However, the reaction temperature was again difficult to precisely control leading to syntheses with slightly different reaction temperatures and thus different mean IONPs size: 23 nm at 330°C and 26 nm at 331°C and 336°C.

Table 1. Results obtained using the second protocol P20_2 and commercial FeSt₃. T1 represents the temperature within the flask during the initial stage for dissolving the reagent and T2 represents the final temperature within the flask during the second stage of IONPs growth.

Synthesis	NP_P20_2_DBE_A	NP_P20_2_DBE_B	NP_P20_2_DBE_C
			
FeSt ₃	FeSt ₃ -TCl	FeSt ₃ -TCl	FeSt ₃ -TCl
T1 (°C)	123	123	126
T2 (°C)	327	331	336
Mean TEM size (nm)	23.2 ± 2.2	26.1 ± 2.2	26.0 ± 1.7
XRD crystallite size (nm)	17.3 ± 1	18.5 ± 1	26.5 ± 1
Lattice parameter (Å)	8.395 ± 0.001	8.393 ± 0.001	8.393 ± 0.001

Syntheses at various temperatures were also performed to assess the impact on reaction outcomes. It was found that the mean diameter of IONPs increased with reaction temperature (Figure 2A), highlighting the stability and consistency of syntheses using commercial FeSt₃. Conversely, inconsistent results were observed when using homemade FeSt₃ at different temperatures. This reaffirms the choice of commercial FeSt₃ as the iron precursor. Nonetheless, variations in the composition of IONPs were noted depending on the reaction temperature.



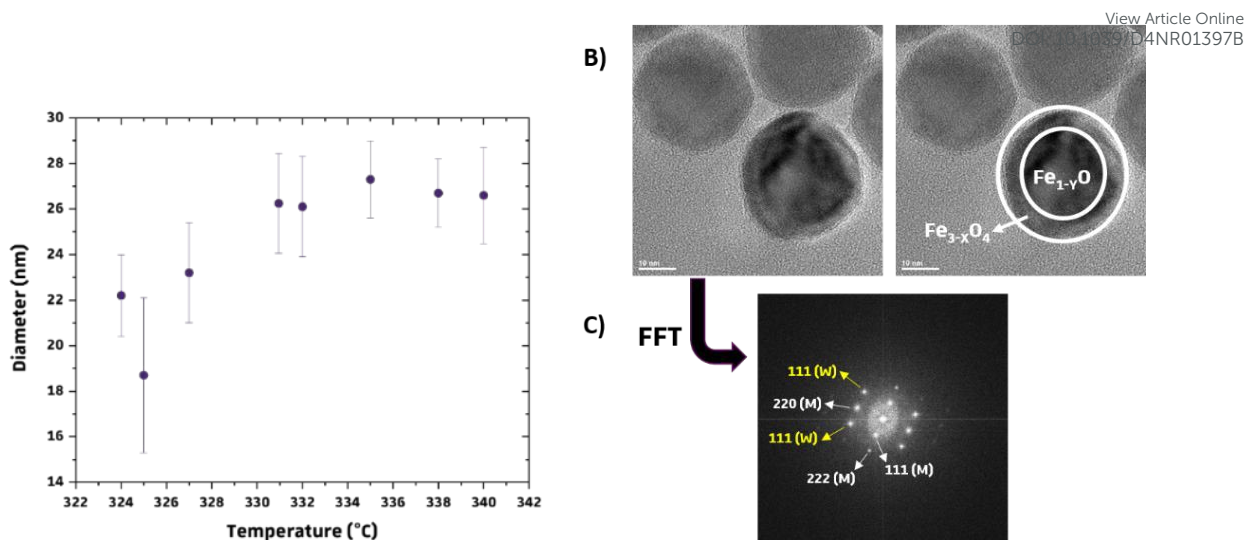


Figure 2. A) Mean diameter of IONPs synthesized using protocol P20_2 as a function of the reaction temperature, B) HRTEM images of core-shell $Fe_{1-x}O@Fe_{3-x}O_4$ IONPs and C) its corresponding FFT pattern with planes indication (W= wüstite plan, M= magnetite plan). (A).

When IONPs are synthesized below 325°C (Table 1), both wüstite and spinel phases are observed in most batches (Figure S4), with both phases present in all batches below 322°C. High-resolution TEM confirmed a core-shell structure (Figures 2B-C), with surface layers exhibiting different crystallographic structures compared to the core. FFT filtering of HRTEM images identified crystallographic planes for both phases (Figure 2B and 2C). These results confirm the formation of a wüstite nucleus under these conditions^{31,32,38}. A reaction temperature above 325°C is necessary for obtaining NPs with a mean size of 23-26 nm and an iron oxide spinel composition. Dendronization is feasible with these IONPs synthesized with a shorter heating duration. Protocol P20_2 is suitable for synthesizing ~20-25 nm IONPs with a monodisperse size distribution and a spinel structure if the reaction temperature is strictly above 325°C.

III.3 Introduction of defects within IONPs by tuning the synthesis conditions

The impact of dibenzyl ether (DBE) on NP synthesis, particularly regarding NP composition, oxidation process, and defect formation, was further investigated. During IONPs synthesis, it has been assessed that the nuclei are constituted of $Fe_{1-x}O$ ^{31,32} and the formation of such $Fe_{1-x}O$ nuclei is again confirmed by these experiments with 0.5 mL of DBE and 19.5 mL of squalene. To achieve spinel iron oxide composition, synthesis conditions need to favor the oxidation kinetics of the wüstite phase. Strategies such as adjusting heating rates³¹ or employing a "nonaqueous redox phase tuning"^{36,37} method involving DBE as oxidizing agent facilitate defect-free NP synthesis. However, DBE's low boiling point limits NP size. Mixing DBE with hydrocarbon solvents enables the production of nearly defect-free NPs in the 10-30 nm range. Additionally, it was found that dense oleic acid (OA) coatings on NP surfaces inhibit oxidation kinetics, while byproducts from DBE thermolysis^{36,37,41} can disrupt these coatings, thereby promoting oxidation kinetics³¹.

To avoid potentially harmful byproducts in biomedical applications, a synthesis method without DBE has been developed consisting in employing a slower heating rate and introducing a nucleation step around 280°C to favor oxidation kinetics over growth kinetics and/or enhance the oxidation of nuclei



before their growth. In addition, as DBE influences the oxidation process limiting the defect formation in resulting IONPs, by omitting DBE, we can produce IONPs with varying defect levels, offering insights into their MH and PTT properties. DBE also influences the shape and composition of IONPs, favoring a uniform spinel structure. We have investigated the impact of DBE quantity, heating rate, and nucleation step on the size, composition, and defects of IONPs.

The influence of varying volumes of DBE on the shape and oxidation kinetics of IONPs was assessed using the P20_2 protocol (Table S2). Increasing DBE volume reduced reaction temperature due to its lower boiling point compared to squalane (298°C versus 450°C). Pure DBE hindered the synthesis of significant-sized IONPs, while creating an oxidizing environment. Adding DBE in volumes up to 1mL resulted in NPs with an average size of 27-32 nm and a spinel composition, promoting size uniformity and oxidation. Further increase in DBE volume produced more faceted, smaller NPs, resembling cubic shapes, consistent with previous studies^{8,37}. The lower reaction temperature and by-products from DBE thermolysis contributed to smaller NPs and a maghemite-like composition. Mixing equal volumes of squalane and DBE yielded well-defined, homogeneous NPs but was deemed less ideal due to safety concerns with the mixture's instability at high temperatures. The ratio of crystallite size to TEM size indicated a positive impact of DBE, although some synthesis conditions introduced an oxidized layer with defects.

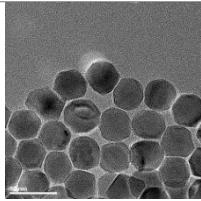
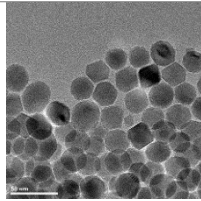
To maintain size homogeneity and enhance oxidation kinetics during synthesis of IONPs with a spinel composition akin to magnetite, incorporating a minimal amount of DBE (0.5 to 1 mL) is necessary due to its crucial role in the oxidation process. Magnetite composition is preferred for its higher M_s and protection against further oxidation is provided by the dendronization thanks to the presence of the two anchoring phosphonate groups^{33,42}. Efforts have been then made to adjust the protocol to improve oxidation kinetics without relying on DBE while ensuring size uniformity.

The syntheses have been thus conducted by implementing a slower heating rate and incorporating a nucleation step in order to establish a better equilibrium between the growth and oxidation kinetics without relying on an oxidizing component like DBE. The nucleation step was set at 280°C for 30 min, based on FeSt_3 TGA/DTA curves (Figure 2) and prior studies^{31,32,39,43,44}. The heating rate was reduced to 1°C/min, down from 5°C/min, until the 60-minute growth stage at 330°C. This revised method, labeled P20_3, was evaluated with and without DBE, with results summarized in Table 2. It enables the synthesis of spherical IONPs with a spinel composition and significant average size, eliminating the need for DBE. However, particle size uniformity is slightly reduced compared to the P20_2 protocol, with sizes exceeding 20 nm, adjustable via reaction temperature.

Table 2. Results obtained with the protocol P20_3 with and without DBE. T1 represents the temperature with the flask during the first step to dissolve reagent, $T_{\text{nucleation}}$ represents the temperature within the flask during the nucleation step, and T2 represents the final temperature within the flask during the second step of IONPs growth.

Synthesis	With DBE	Without DBE
-----------	----------	-------------



		
FeSt ₃	FeSt ₃ -TCl	FeSt ₃ -TCl
T1 (°C)	121	121
T _{nucleation} (°C)	285	282
T2 (°C)	329	326
Mean TEM size (nm)	33.3 ± 3.2	25.4 ± 3.0
XRD crystallite size (nm)	26.2 ± 1	23.3 ± 1
Lattice parameter (Å)	8.391 ± 0.001	8.393 ± 0.001
Ratio crystallite size on TEM size	0.79	0.929

The composition's homogeneity is crucial, being evident from comparable XRD patterns of both batches (Figure S5), showing similar characteristics, predominantly iron oxide spinel peaks with lattice parameters akin to magnetite. However, a faint XRD peak in NP_P20_3_no_DBE suggests a minor presence of wüstite phase. Introduction of DBE leads to larger IONPs (>30 nm), possibly altering nucleation and growth. Reproducibility studies reported in Table S3 confirmed promising results with lower reaction temperature, albeit slightly more heterogeneous size distribution compared to previous protocol (P20_2). Additionally, the ratio of crystallite size to TEM size indicates the presence of defects in these IONPs.

The P20_3_no_DBE protocol allowed for the synthesis of uniform 20-25 nm IONPs without using DBE. However, careful temperature control is still essential to maintain composition uniformity, as low temperatures can hinder wüstite core oxidation. Our study confirms the feasibility of synthesizing these nanoparticles with or without DBE. When DBE is omitted, there is a slight reduction in size uniformity, which is not expected to significantly affect magnetic properties. Nonetheless, its absence may affect oxidation kinetics, potentially altering nanoparticle defect levels.

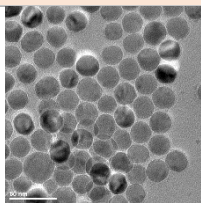
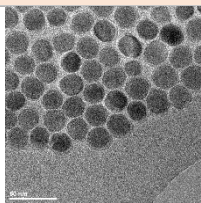
Oxidized core-shell IONPs

Two protocols were established to produce 20-25 nm spherical IONPs with consistent spinel composition but varying levels of defects. Despite this, various synthesis methods can yield core-shell spherical IONPs with a wüstite core and magnetite shell. Exploring the potential of subjecting these batches to thermal treatment to oxidize the wüstite phase into magnetite and potentially modify defect levels, 22 nm spherical IONPs (NP_CS) with a Fe_{1-y}O@Fe_{3-x}O₄ core-shell structure were oxidized, resulting in NP_CS_ox. In brief, 5 mL of IONPs suspension in THF were mixed with 5 mL of oleic acid (OA) and stirred for 30 minutes at 120°C. TEM size, lattice parameters, and crystallite size of NP_CS and NP_CS_ox were compared via XRD refinement (Table 3), alongside results from established protocols P20_2 and P20_4_no_DBE. XRD diffractograms (Figure S6) and refinement data



(Table 3) show disappearance of the wüstite phase following post-oxidation, suggesting the potential of core-shell synthesis with thermal treatment.

Table 3. Comparison of mean TEM size, crystallite size and lattice parameters of a core shell IONPs batch ($Fe_{1-y}O@Fe_{3-x}O_4$) before and after oxidation treatment.

Synthesis	NP_CS	NP_CS_ox
		
FeSt ₃	FeSt ₃ -TCI	FeSt ₃ -TCI
Mean TEM size (nm)	22.6 ± 2.3	23.2 ± 1.7
XRD crystallite size (nm)	/	18.3 ± 1
Lattice parameter (Å)	/	8.393 ± 0.001
Ratio crystallite size on TEM size	/	0.79

III.4 Evaluation of the defect's amount in IONPs

The demand to quantify defects in IONPs has grown due to their impact on MH and PTT treatments. Various methods exist for characterizing IONPs to evaluate defects. X-ray pattern refinement determines crystallite size, reflecting the size of the diffracting domain. A NP's crystallite size typically matches its TEM size if it is monocrystalline. However, structural defects can create smaller crystalline domains. A NP with few defects shows a close match between crystallite and TEM sizes, while numerous defects result in a smaller crystallite size. Comparing these sizes allows for an initial assessment of defects, but other techniques should be used for accuracy, considering variations in measurement methods. Table 4 compares this ratio for batches from different synthesis methods, providing initial insights into potential structural defects.

Table 4. Comparison between mean crystallite size and TEM size from various batches synthesized with P20_2 and P20_3_no_DBE protocols.

	TEM size (± 2 nm)	Crystallite size (± 1 nm)	Ratio	Mean ratio
NP_P20_2 (with DBE)	26.6	25.2	0.95	0.96 ± 0.06
	22.2	19.3	0.87	
	26.7	26.5	0.99	
	26.0	26.5	1.01	
NP_P20_3_no_DBE	23.9	23.4	0.98	0.85 ± 0.09



(without DBE)	22.9	19.2	0.84	View Article Online DOI: 10.1039/D4NR01397B
	23.7	17.8	0.75	
	18.0	15.2	0.84	
NP_P20_CS_ox	23.2	18.3	0.79	/

Comparing crystallite sizes to determine defect amounts is challenging due to sample variability in size from the P20_3_no_DBE protocol. Among eight samples from two synthesis protocols, NPs from the P20_2 protocol (with DBE) show closely aligned average crystallite sizes with TEM measurements. Additionally, their crystallite size ratio consistently indicates fewer defects, confirming DBE's role in creating an oxidizing environment during synthesis, favorable for fewer defects in IONPs. The oxidation treatment of core-shell IONPs yields a slightly lower ratio than that of P20_3_no_DBE batches, suggesting that the oxidation promoted defects as expected.

The HRTEM images show crystallographic planes in the studied IONPs, with FFT revealing irregularities like stacking faults or dislocations (Figure 3)^{7,33}. In Figure 3, inverse FFT results from magnetite lattice planes (111) and (222) in IONPs synthesized with P20_2 and P20_3_no_DBE protocols are compared. Notably, P20_3_no_DBE protocol showed a higher prevalence of defects, particularly edge dislocations, compared to P20_2. While the analysis is not quantitative, it strongly suggests that IONPs from P20_3_no_DBE protocol have qualitatively more defects than those from P20_2 protocol.

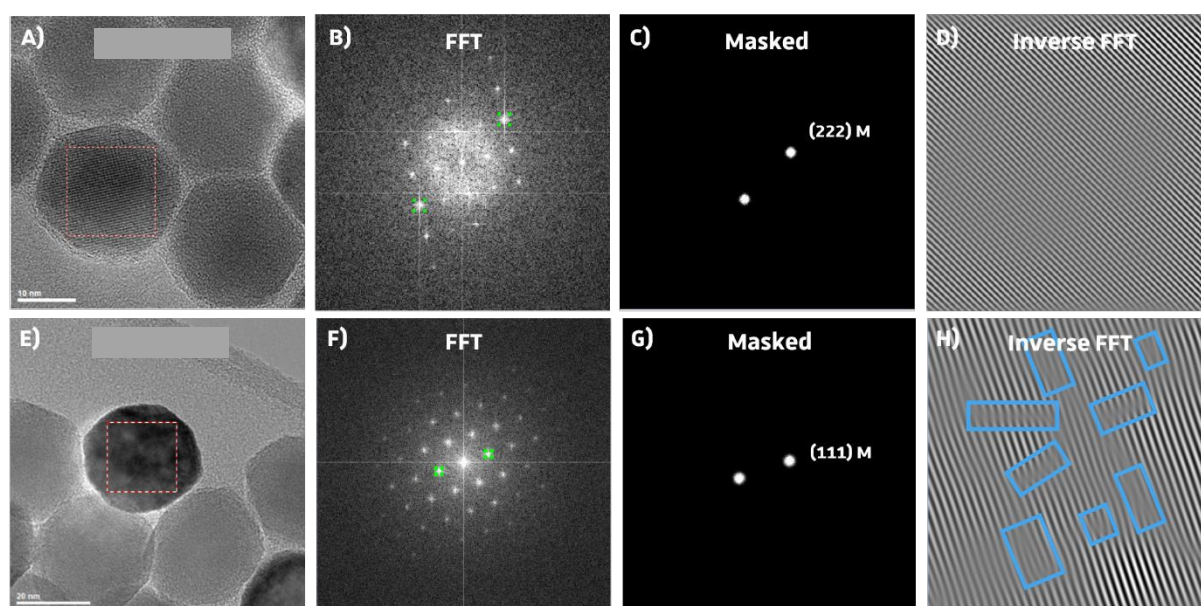


Figure 3: Up row corresponds to IONPs synthesized with protocol P20_2 and lower row corresponds to IONPs synthesized with protocol P20_3_no_DBE. A) and E) High resolution TEM images of IONPs, B) and F) the corresponding FFT images, C) and G) applied masked on two reflections plans, and D) and H) inverse FFT to visualize the crystallographic planes and eventual defects. Blue squares show crystallographic defects.

A comparative analysis was conducted to determine the band gap and Urbach energy (Figure S7 and Table 5) of various batches of IONPs from their UV-VIS spectra (Figure S8). Urbach energy (E_u)



levels are closely related to the presence of defects^{45,46}, particularly in semiconductor oxides like magnetite, where localized defect states^{30,47}, such as oxygen vacancies, can reduce the band gap. Higher E_u values (Figures S7-9) indicate more defects, suggesting an imperfect conduction band^{26,45,47,48}. The band gap energy remains consistent across samples (3.5 ± 0.2 eV), but significant differences in E_u are observed between batches synthesized with and without DBE. Samples synthesized with DBE show lower E_u values, indicating fewer defects from oxygen vacancies. Attempts to replicate the effects of DBE by altering synthesis parameters (P20_3_no_DBE protocol) result in spinel structure NPs with both point and structural defects. Urbach energy increases notably in samples synthesized after an oxidation treatment, likely due to more oxidation sites from the wüstite core oxidation process.

Table 5: Calculated E_g and E_u from various batches synthesized with P20_2 and P20_3_no_DBE protocols.

Protocol	Batch	E_g (± 0.2 eV)	E_u (eV)
P20_2 (with DBE)	NP_P20_DB_E_1	3.4	0.6
	NP_P20_DB_E_2	3.5	0.7
	NP_P20_DB_E_3	3.7	0.7
P20_3_no_DB_E (without DBE)	NP_P20_NO_DB_E_1	3.5	1.2
	NP_P20_NO_DB_E_2	3.4	1.2
	NP_P20_NO_DB_E_3	3.4	0.9
Oxidation process	NP_CS_ox	3.4	1.4

III.5 Magnetic properties and heating capabilities of IONPs suspensions

The impact of wüstite core, spinel composition, and defect amount on magnetic properties and heating abilities of 20-25 nm spherical IONPs were investigated. This included IONPs from protocols P20_2 and P20_3_no_BDE (NP_20_DB_E and NP_20_no_BDE), core-shell IONPs (NP_20_CS), and their oxidized counterparts (NP_20_CS_ox). Magnetic properties were initially measured using SQUID (Figure 4). Heating capabilities were then studied via MH after dendronization of IONPs, which colloidal stability was assessed by DLS measurements (Figure S10).



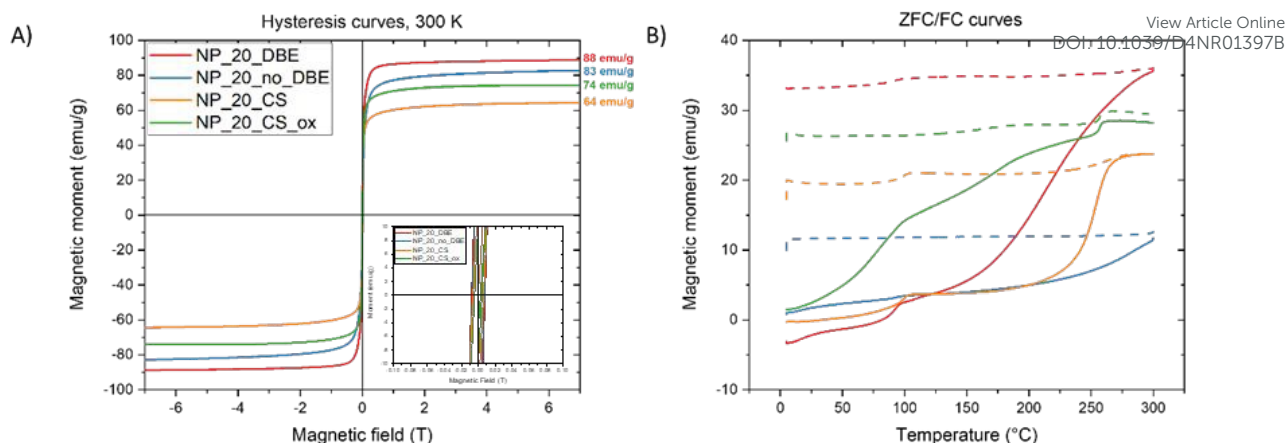


Figure 4: A) Magnetization curves (insert: zoom between -0.1 et 0.1 T) and B) ZFC/FC curve of four types of IONPs.

All samples show quite a superparamagnetic behavior at 300 K (Figure 4A) with a very small hysteresis with a coercive field lower than 0.01T). NP_20_DBE and NP_20_no_DBE exhibit high M_s values of 88 $\text{emu}\cdot\text{g}^{-1}$ and 83 $\text{emu}\cdot\text{g}^{-1}$ respectively, close to bulk magnetite (94 $\text{emu}\cdot\text{g}^{-1}$). The core-shell sample also demonstrates a high M_s of 64 $\text{emu}\cdot\text{g}^{-1}$, increasing to 74 $\text{emu}\cdot\text{g}^{-1}$ upon post-oxidation treatment. ZFC and FC curves (Figure S4B) reveal high blocking temperatures typical for IONPs of this size range (20-50 nm) due to significant dipolar interactions⁴⁹. For the NP_20_DBE sample, there is a noticeable increase in magnetization around 90 K in both the ZFC and FC curves. This increase is attributed to the Verwey transition, which is a characteristic feature of magnetite. The shift of the Verwey transition temperature below 110 K (the usual value for MNPs) has been linked to non-stoichiometric magnetite caused by the presence of Fe^{2+} vacancies⁵⁰. The onset of the Verwey transition is nearly undetectable in the NP_20_no_DBE sample. In contrast, it is quite evident in the core-shell sample. Additionally, the core-shell sample shows a significant increase in magnetization between 225 and 275 K. This feature cannot be related to the Néel transition of wüstite, which is expected around 200 K, but is instead attributed to a highly "disordered" magnetic phase referred to as the X-phase by other groups^{51,52}. In the oxidized sample, the Verwey transition becomes more prominent than the X-phase transition, indicating the dominance of the magnetite phase, as reflected in the increased M_s .

In the initial stage of MH study, the heat generation capabilities of four types of iron oxide nanoparticles (IONPs) suspended in water (1 $\text{mg}_{\text{Fe}}/\text{mL}$) were examined. Specific Absorption Rate (SAR) values were plotted against the amplitude (H) of Alternating Magnetic Field (AMF), ranging from 5kA/m to 60 kA/m, at a fixed frequency of 355 kHz. To ensure accuracy, the contribution from pure water at each H was subtracted. IONPs from the NP_20_CS batch, with a core-shell architecture, showed moderate SAR values, increasing slightly with H from 75 $\text{W}/\text{g}_{\text{Fe}}$ at 5kA/m to 475 $\text{W}/\text{g}_{\text{Fe}}$ at 60 kA/m. In contrast, NP_20_CS_ox exhibited a significant enhancement in heating performance, with SAR values nearly doubling at each H value, ranging from 130 $\text{W}/\text{g}_{\text{Fe}}$ to 850 $\text{W}/\text{g}_{\text{Fe}}$ as H increased. This improvement is attributed to the conversion of the magnetically inactive wüstite core into magnetite/maghemite. IONPs produced using the P20_3_no_BDE protocol, containing defects within their structure and exhibiting a high M_s value, showed higher SAR values over the entire H range



compared to previous IONPs, ranging from 80 W/g_{Fe} to 1525 W/g_{Fe}. The presence of defects within the spinel structure contributed to this increase. IONPs from the NP_20_DBE batch, with reduced defects in their spinel structure and the highest M_s value, yielded the highest SAR values, reaching 1680 W/g_{Fe} at 30 kA/m and 2150 W/g_{Fe} at 60 kA/m. These IONPs demonstrate significantly enhanced heating capabilities, surpassing established or revised safety limits for magnetic hyperthermia treatment, with SAR values of 780 W/g_{Fe} at 15 kA/m and 1470 W/g_{Fe} at 25 kA/m.

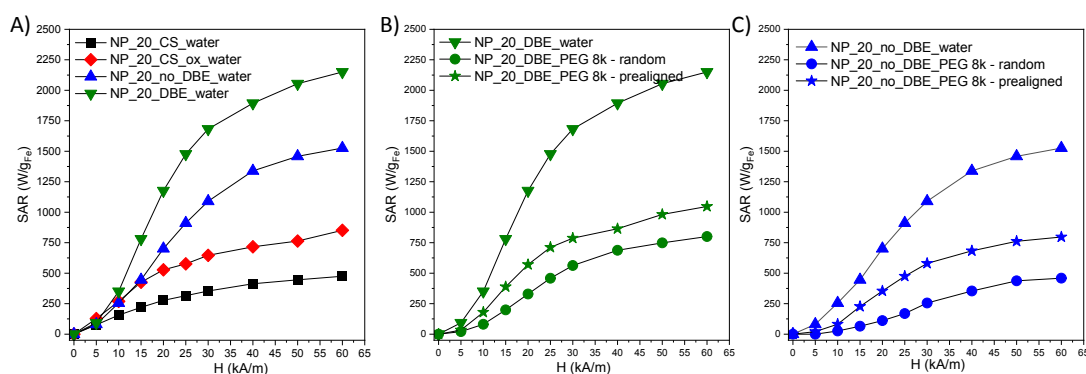


Figure 5. A) SAR values for NP_P20_DBE, NP_P20_no_DBE, NP_20_CS and NP_20_CS_ox suspensions in water and of B) NP_20_DBE and C) NP_20_no_DBE suspended in water and in PEG8k matrix, random or prealigned, at a concentration of 1 mg_{Fe}/mL.

Based on the above analysis, IONPs produced using both P20_2 and P20_3_no_DBE protocols are promising for further in vitro and in vivo MH studies. However, within cells, IONPs are confined to lysosomes, limiting their Brownian motion and relying solely on Neel relaxation for heating. To investigate this, IONPs were immobilized in a PEG8k matrix, either randomly or prealigned under a static magnetic field (strength of 65 kA/m). SAR values significantly decrease when IONPs are immobilized in PEG, reducing Brownian motion by 68% for NP_P20_DBE and 78% for NP_P20_3_no_DBE (Figures 5B and 5C). When the IONPs are prealigned within the solid matrix with their easy axis of magnetization being parallel to AMF lines, the Neel contribution is increased, restoring SAR values by up to 50% compared to water (Figures 5B and 5C). However, one may notice that even if the SAR values of IONPs with DBE decrease when they are immobilized, they stay always higher than those of IONPs without DBE. Therefore, IONPs with DBE are the most performant for MH.

For photothermal experiments, suspensions of IONPs at 0.05 mg_{Fe}/mL in chloroform were exposed to a 1064 nm laser at 1 W/cm² for 3 minutes. A chloroform-only sample served as a control. Temperature was monitored continuously, and temperature changes over time were plotted. IONPs consistently led to significant temperature increases compared to the control. However, discerning a clear trend between synthesis protocols P20_2 and P20_3_no_DBE was challenging, as their temperature-time curves showed similar patterns. Nonetheless, batches synthesized with DBE (P20_2) generally exhibited slightly higher temperature increases compared to those without DBE (P20_3_no_DBE).

Table 6. SAR values by photothermia of IONPs synthesized with the P20_2 and P20_3_no_DBE protocols (1064 nm, 1W.cm⁻²) at a concentration of 0.05 mg_{Fe}/mL.



Protocol	Batch	SAR (W.g ⁻¹)	E _u (± 0.2 eV)
P20_2	NP_P20_2_DBE_2	548	0.6
	NP_P20_2_DBE_3	540	0.7
P20_3_no_DBE	NP_P20_3_no_DBE_1	412	1.2
	NP_P20_3_no_DBE_3	497	0.9

View Article Online
DOI: 10.1039/D4NR01397B

Comparing SAR values (Table 6), batches synthesized with the P20_2 protocol show slightly higher values than those with P20_3_no_DBE and a correlation of SAR values with the Urbach energy is observed³⁰. The SAR values decrease when Urbach energy increases but for an Urbach energy of 0.6, the SAR value is 548 W/g when it is 412 W/g when the energy is two times higher. Further measurements on broader range of Urbach energy are recommended to confirm this correlation between vacancies defect levels and PTT efficiency. However, IONPs with DBE exhibit notable heating properties even at low concentrations (0.05 mg_{Fe}/mL).

MH measurements indicated that SAR values of IONPs in suspension increase with M_s values, primarily due to Brownian relaxation. Experiments with immobilized IONPs confirmed that defects favor Neel relaxation^{7,23}. However, IONPs synthesized with DBE with less defects, displayed higher SAR values even when immobilized in a matrix and they are thus preferable for both *in vitro* and *in vivo* MH applications. Regarding PTT measurements, an impact of defects and especially a correlation with Urbach energy is noted suggesting thus an impact of defects³⁰. Consequently, the protocol utilizing DBE in our experimental conditions and leading to fewer defects appears optimal for achieving IONPs with superior performance in both MH and PTT.

IV Conclusion

The objectives were to synthesize IONPs with a mean size of 20-25 nm and a spinel composition exhibiting different "amount" of defects as defects were more and more demonstrated to impact MH and PTT performances. The synthesis of IONPs with a mean size higher than 20 nm and a spinel composition by the thermal method is always challenging as nuclei with a wüstite composition are formed and thus there is a big issue in controlling both the grain growth and the oxidation kinetics after the nucleation step. The most used approach to face this problem is the addition of DBE, an oxidizing agent, in the reaction media, which allows avoiding to obtain core-shell structure with a wüstite core and a spinel iron oxide shell and leads to defect free iron oxide spinel NPs. However, DBE can introduce harmful by-products. Therefore, we have tuned different synthesis parameters using the thermal decomposition method to try to avoid DBE and the most important objective here was to synthesize IONPs with a spinel composition and different defects density.

Commercial iron stearate precursor was chosen for reproducibility over homemade ones due to the difficulty in controlling the complex polycation distributions in home-made precursors. Various protocols were tested, revealing optimal conditions of 1 hour reaction duration and 330°C reaction temperature to avoid core-shell structure formation. The significance of DBE as an oxidizing agent in producing defect-free IONPs was emphasized by varying its quantity. It was observed that using approximately 0.5 or 1 mL of DBE was adequate to produce IONPs sized around 20-25 nm with a



spinel composition. Higher amounts of DBE led to IONPs with cubic shapes and a magnetite composition. Additionally, experiments involving a slower heating rate and a nucleation step, with or without DBE, showed that this protocol could yield IONPs with a spinel composition even in the absence of DBE. Consequently, two distinct protocols have been established for synthesizing IONPs with an average size between 20-25 nm, with or without DBE.

The magnetic measurements indicated that IONPs synthesized with DBE had higher M_s values compared to those synthesized without DBE, suggesting a composition similar to magnetite. Structural defects were examined using XRD and HRTEM, while point defects like vacancies were assessed by calculating Urbach energy from UV spectra. IONPs synthesized without DBE exhibited more structural defects and higher Urbach energies, indicating the presence of more point defects, in contrast to those synthesized with DBE.

MH and PTT experiments were conducted to evaluate how defects in the spinel structure affect hyperthermia performance. Both experiments indicated that IONPs without defects would display enhanced PTT and MH SAR values. Specifically, IONPs synthesized with DBE showed higher SAR values due to reduced defect content and higher M_s , but SAR values halved when immobilized in a solid matrix. IONPs synthesized without DBE, with more defects, had lower SAR values, but the decrease was less pronounced when immobilized in the solid matrix, indicating less influence of Brownian relaxation. However, even if the SAR values of IONPs with DBE decrease when they are immobilized in a matrix, the SAR values stay higher than those of IONPs synthesized without DBE. PTT measurements showed slightly larger SAR values for IONPs with DBE compared to those without and a correlation is noticed. Other results on broader range of Urbach energy would be necessary to unambiguously conclude about this correlation. Therefore, IONPs synthesized with DBE exhibiting fewer defects are the most performant ones to combine both MH and PTT in one formulation.

Conflicts of interest statement. There is no conflict of interest to declare.

Data availability. The data supporting this article have been included as part of the Supplementary Information

Funding. The Region Alsace, France, and the University of Mons are gratefully acknowledged for the doctoral fellowship to Barbara Freis. This project received funding from ANR (EURONANOMED2020-121 - THERAGET) under the umbrella of the ERA-NET EuroNanoMed (GA N°723770) of the EU Horizon 2020 Research and Innovation, from Alsace contre le Cancer and ProtherWal "Walloon Region via the ProtherWal Society (Agreement 7289). SuperBranche is thanked for providing dendron molecules. UMONS acknowledges the financial support of the Fond National de la Recherche Scientifique (FNRS), the ARC Programs of the French Community of Belgium, COST actions and the Walloon region (ProtherWal and Interreg projects).

Acknowledgments. The authors thank the XRD and TEM platform of IPCMS and Dr Vasiliki Papaefthymiou of ICPEES for XPS measurement



References:

- 1 G. Cotin, C. B.- Andujar, D. V. Nguyen, C. Affolter-Zbaraszczuk, S. Boutry, A. BOOS, P. Ronot, B. Uring, P. Choquet, P. E. Zorn, D. Mertz, S. Laurent, R. N. Muller, F. Meyer, D. Felder-Flesch and S. Begin, *Nanotechnology*, DOI:10.1088/1361-6528/ab2998.
- 2 C. Blanco-Andujar, A. Walter, G. Cotin, C. Bordeianu, D. Mertz, D. Felder-Flesch and S. Begin-Colin, *Nanomedicine (London, England)*, 2016, **11**, 1889–1910.
- 3 A. E. Deatsch and B. A. Evans, *Journal of Magnetism and Magnetic Materials*, 2014, **354**, 163–172.
- 4 A. Espinosa, R. Di Corato, J. Kolosnjaj-Tabi, P. Flaud, T. Pellegrino and C. Wilhelm, *ACS Nano*, 2016, **10**, 2436–2446.
- 5 S. Cabana, A. Curcio, A. Michel, C. Wilhelm and A. Abou-Hassan, *Nanomaterials*, 2020, **10**, 1548.
- 6 B. Freis, G. Cotin, F. Perton, D. Mertz, S. Boutry, S. Laurent and S. Begin-Colin, in *Magnetic Nanoparticles in Human Health and Medicine*, 2021, pp. 380–429.
- 7 G. Cotin, C. Blanco-Andujar, F. Perton, L. Asín, J. M. de la Fuente, W. Reichardt, D. Schaffner, D.-V. Ngyen, D. Mertz, C. Kiefer, F. Meyer, S. Spassov, O. Ersen, M. Chatzidakis, G. A. Botton, C. Hénoumont, S. Laurent, J.-M. Greneche, F. J. Teran, D. Ortega, D. Felder-Flesch and S. Begin-Colin, *Nanoscale*, 2021, **13**, 14552–14571.
- 8 P. Guardia, R. Di Corato, L. Lartigue, C. Wilhelm, A. Espinosa, M. Garcia-Hernandez, F. Gazeau, L. Manna and T. Pellegrino, *ACS Nano*, 2012, **6**, 3080–3091.
- 9 R. D. Corato, A. Espinosa, L. Lartigue, M. Tharaud, S. Chat, T. Pellegrino, C. Ménager, F. Gazeau and C. Wilhelm, 2014, **12**.
- 10 A. Hervault and N. T. K. Thanh, *Nanoscale*, 2014, **6**, 11553–11573.
- 11 W. Baaziz, B. P. Pichon, S. Fleutot, Y. Liu, C. Lefevre, J.-M. Greneche, M. Toumi, T. Mhiri and S. Begin-Colin, *J. Phys. Chem. C*, 2014, **118**, 3795–3810.
- 12 G. Cotin, C. Kiefer, F. Perton, D. Ihiwakrim, C. Blanco-Andujar, S. Moldovan, C. Lefevre, O. Ersen, B. Pichon, D. Mertz and S. Bégin-Colin, *Nanomaterials*, 2018, **8**, 881.
- 13 J. Santoyo Salazar, L. Perez, O. de Abril, L. Truong Phuoc, D. Ihiwakrim, M. Vazquez, J.-M. Greneche, S. Begin-Colin and G. Pourroy, *Chemistry of Materials*, 2011, **23**, 1379–1386.
- 14 A. Sathya, P. Guardia, R. Brescia, N. Silvestri, G. Pugliese, S. Nitti, L. Manna and T. Pellegrino, *Chemistry of Materials*, 2016, **28**, 1769–1780.
- 15 M. Levy, A. Quarta, A. Espinosa, A. Figuerola, C. Wilhelm, M. García-Hernández, A. Genovese, A. Falqui, D. Alloyeau, R. Buonsanti, P. D. Cozzoli, M. A. García, F. Gazeau and T. Pellegrino, *Chem. Mater.*, 2011, **23**, 4170–4180.
- 16 F. Gazeau, M. Lévy and C. Wilhelm, *Nanomedicine (London, England)*, 2008, **3**, 831–844.
- 17 J. Mohapatra, A. Mitra, D. Bahadur and M. Aslam, *CrystEngComm*, 2013, **15**, 524–532.
- 18 J. G. Ovejero, D. Cabrera, J. Carrey, T. Valdivielso, G. Salas and F. J. Teran, *Phys. Chem. Chem. Phys.*, 2016, **18**, 10954–10963.
- 19 D. Cabrera, A. Coene, J. Leliaert, E. J. Artes, N. D. Telling and F. J. Teran, *ACS Nano*, 2018, **12**.
- 20 C. Iacovita, G. F. Stiufiuc, R. Dudric, N. Vedeanu, R. Tetea, R. I. Stiufiuc and C. M. Lucaciu, *Magnetochemistry*, 2020, **6**, 23.
- 21 C. Iacovita, R. Stiufiuc, T. Radu, A. Florea, G. Stiufiuc, A. Dutu, S. Mican, R. Tetea and C. M. Lucaciu, *Nanoscale Res Lett*, 2015, **10**, 391.



- 22 D. Soukup, S. Moise, E. Céspedes, J. Dobson and N. D. Telling, *ACS Nano*, 2015, **9**, 231–240. [View Article Online](#)
DOI: 10.1039/D4NR01397B
- 23 A. Lak, M. Cassani, B. T. Mai, N. Winckelmans, D. Cabrera, E. Sadrollahi, S. Marras, H. Remmer, S. Fiorito, L. Cremades-Jimeno, F. J. Litterst, F. Ludwig, L. Manna, F. J. Teran, S. Bals and T. Pellegrino, *Nano Letters*, 2018, **18**, 6856–6866.
- 24 A. Lappas, G. Antonaropoulos, K. Brintakis, M. Vasilakaki, K. N. Trohidou, V. Iannotti, G. Ausanio, A. Kostopoulou, M. Abeykoon, I. K. Robinson and E. S. Bozin, *Phys. Rev. X*, 2019, **9**, 041044.
- 25 A. Lak, S. Disch and P. Bender, *Advanced Science*, 2021, **8**, 2002682.
- 26 M. E. Sadat, M. Kaveh Baghbador, A. W. Dunn, H. P. Wagner, R. C. Ewing, J. Zhang, H. Xu, G. M. Pauletti, D. B. Mast and D. Shi, *Applied Physics Letters*, 2014, **105**, 091903.
- 27 T.-J. Yu, P.-H. Li, T.-W. Tseng and Y.-C. Chen, *Nanomedicine*, 2011, **6**, 1353–1363.
- 28 A. Espinosa, J. Kolosnjaj-Tabi, A. Abou-Hassan, A. Plan Sangnier, A. Curcio, A. K. A. Silva, R. Di Corato, S. Neveu, T. Pellegrino, L. M. Liz-Marzán and C. Wilhelm, *Adv. Funct. Mater.*, 2018, **28**, 1803660.
- 29 C. Lozano-Pedraza, E. Plaza-Mayoral, A. Espinosa, B. Sot, A. Serrano, G. Salas, C. Blanco-Andujar, G. Cotin, D. Felder-Flesch, S. Begin-Colin and F. J. Teran, *Nanoscale Adv.*, 2021, **3**, 6490–6502.
- 30 E. Bertuit, E. Benassai, G. Mériduet, J.-M. Greneche, B. Baptiste, S. Neveu, C. Wilhelm and A. Abou-Hassan, *ACS Nano*, 2022, **16**, 271–284.
- 31 G. Cotin, F. Pertont, C. Petit, S. Sall, C. Kiefer, V. Begin, B. Pichon, C. Lefevre, D. Mertz, J.-M. Greneche and S. Begin-Colin, *Chem. Mater.*, 2020, **32**, 9245–9259.
- 32 G. Cotin, B. Heinrich, F. Pertont, C. Kiefer, G. Francius, D. Mertz, B. Freis, B. Pichon, J. Strub, S. Cianféran, N. Ortiz Peña, D. Ihiawakrim, D. Portehault, O. Ersen, A. Khammari, M. Picher, F. Banhart, C. Sanchez and S. Begin-Colin, *Small*, 2022, 2200414.
- 33 A. Walter, C. Billotey, A. Garofalo, C. Ulhaq-Bouillet, C. Lefèvre, J. Taleb, S. Laurent, L. Vander Elst, R. N. Muller, L. Lartigue, F. Gazeau, D. Felder-Flesch and S. Begin-Colin, *Chemistry of Materials*, 2014, **26**, 5252–5264.
- 34 B. P. Pichon, O. Gerber, C. Lefevre, I. Florea, S. Fleutot, W. Baaziz, M. Pauly, M. Ohlmann, C. Ulhaq, O. Ersen, V. Pierron-Bohnes, P. Panissod, M. Drillon and S. Begin-Colin, *Chemistry of Materials*, 2011, **23**, 2886–2900.
- 35 E. Wetterskog, C.-W. Tai, J. Grins, L. Bergström and G. Salazar-Alvarez, *ACS Nano*, 2013, **7**, 7132–7144.
- 36 R. Chen, M. G. Christiansen, A. Sourakov, A. Mohr, Y. Matsumoto, S. Okada, A. Jasanoff and P. Anikeeva, *Nano Lett.*, 2016, **16**, 1345–1351.
- 37 P. Guardia, A. Riedinger, S. Nitti, G. Pugliese, S. Marras, A. Genovese, M. E. Materia, C. Lefevre, L. Manna and T. Pellegrino, *Journal of Materials Chemistry B*, 2014, **2**, 4426.
- 38 F. Pertont, G. Cotin, C. Kiefer, J.-M. Strub, S. Cianferani, J.-M. Greneche, N. Parizel, B. Heinrich, B. Pichon, D. Mertz and S. Begin-Colin, *Inorg. Chem.*, 2021, **60**, 12445–12456.
- 39 G. Cotin, C. Kiefer, F. Pertont, M. Boero, B. Özdamar, A. Bouzid, G. Ori, C. Massobrio, D. Begin, B. Pichon, D. Mertz and S. Begin-Colin, *ACS Applied Nano Materials*, 2018, **1**, 4306–4316.
- 40 A. Demortière, P. Panissod, B. P. Pichon, G. Pourroy, D. Guillon, B. Donnio and S. Bégin-Colin, *Nanoscale*, 2011, **3**, 225–232.
- 41 K. E. Gilbert and J. J. Gajewski, *J. Org. Chem.*, 1982, **47**, 4899–4902.



- 42 T. J. Daou, J. M. Grenèche, G. Pourroy, S. Buathong, A. Derory, C. Ulhaq-Bouillet, B. Donnio, D. Guillon and S. Begin-Colin, *Chemistry of Materials*, 2008, **20**, 5869–5875. View Article Online
DOI: 10.1039/D4NR01397B
- 43 S. G. Kwon, Y. Piao, J. Park, S. Angappane, Y. Jo, N.-M. Hwang, J.-G. Park and T. Hyeon, *Journal of the American Chemical Society*, 2007, **129**, 12571–12584.
- 44 L. M. Bronstein, X. Huang, J. Retrum, A. Schmucker, M. Pink, B. D. Stein and B. Dragnea, *Chemistry of Materials*, 2007, **19**, 3624–3632.
- 45 B. Choudhury and A. Choudhury, *Physica E: Low-dimensional Systems and Nanostructures*, 2014, **56**, 364–371.
- 46 H. El Ghandour, H. M. Zidan, M. M. H. Khalil and M. I. M. Ismail, *International Journal of Electrochemical Science*, 2012, **7**, 5734–5745.
- 47 V. R. Akshay, B. Arun, G. Mandal and M. Vasundhara, *Phys. Chem. Chem. Phys.*, 2019, **21**, 12991–13004.
- 48 S. M. Wasim, C. Rincón, G. Marín, P. Bocaranda, E. Hernández, I. Bonalde and E. Medina, *Phys. Rev. B*, 2001, **64**, 195101.
- 49 M. A. Gonzalez-Fernandez, T. E. Torres, M. Andrés-Vergés, R. Costo, P. de la Presa, C. J. Serna, M. P. Morales, C. Marquina, M. R. Ibarra and G. F. Goya, *Journal of Solid State Chemistry*, 2009, **182**, 2779–2784.
- 50 A. R. Muxworthy and E. McClelland, *Geophysical Journal International*, 2000, **140**, 101–114.
- 51 I. Castellanos-Rubio, I. Rodrigo, R. Munshi, O. Arriortua, J. S. Garitaonandia, A. Martinez-Amesti, F. Plazaola, I. Orue, A. Pralle and M. Insausti, *Nanoscale*, 2019, **11**, 16635–16649.
- 52 C. P. Guntlin, S. T. Ochsenein, M. Wörle, R. Erni, K. V. Kravchyk and M. V. Kovalenko, *Chem. Mater.*, 2018, **30**, 1249–1256.



View Article Online
DOI: 10.1039/D4NR01397B

Data availability. The data supporting this article have been included as part of the Supplementary Information

